Performance of the prototype module of the GlueX electromagnetic barrel calorimeter

B.D. Leverington [*], G.J. Lolos, Z. Papandreou, R. Hakobyan, G.M. Huber, K.L. Janzen

Department of Physics, University of Regina, Regina, SK S4S 0A2, Canada

E.B. Scott, M.R. Shepherd

Department of Physics, Indiana University, Bloomington, IN 47405, USA

D.S. Carman, D.W. Lawrence, E.S. Smith, S. Taylor, E.J. Wolin

Thomas Jefferson National Accelerator Facility, Newport News, VA 23606, USA

F.J. Klein, J.P. Santoro, D.I. Sober

Department of Physics, The Catholic University of America, Washington, DC 20064, USA

C. Kourkoumeli

Department of Physics, National and Kapodistrian University of Athens, 157 84 Athens, Greece

Abstract

A photon beam test of the 4 m long prototype lead/scintillating fibre module for the GlueX electromagnetic barrel calorimeter was carried out in Hall B at the Thomas Jefferson National Accelerator Facility with the objective of measuring the energy and timing resolutions of the module as well as the number of photoelectrons generated. Data were collected over an energy range of 150 to 650 MeV at multiple positions and angles along the module. Details of the analysis at the centre of and perpendicular to the module are shown herein; the results are $\sigma_{\Delta T/2} = 70/\sqrt{E}$ ps, $\sigma_E/E = 5.5\%/\sqrt{E}$ and 770 photoelectrons for 1 GeV at each end of the module.

Key words: electromagnetic calorimeter, scintillating fibres
PACS: 29.40 Vj

1 Introduction

The principal aim behind the GlueX experiment is to elucidate the phenomenon of confinement, by conducting advanced meson spectroscopy and searching for predicted exotic hybrid states with explicit gluonic degrees of freedom. Such states have a plethora of decays leading to photons in the final state, and require hermetic calorimetry for their detection and measurement of their four momentum. Test results from the cylindrical electromagnetic calorimeter for GlueX are reported herein.

A brief overview of the GlueX experiment is presented in Section 2. The photon beam test – conducted in Hall B at the Thomas Jefferson National Accelerator facility – and the setup of the experiment are covered in Section 3. The analysis method and results for the energy resolution of the Hall B beam test are described in Section 4. The timing resolution analysis and results are shown in Section 5, while the photoelectron analysis is provided in Section 6. Lastly, the results are summarized in Section 7.

2 Overview of GlueX

To achieve the primary physics goal of GlueX, namely mapping the spectrum of gluonic excitations of light mesons, it is essential to measure photons and charged particles with sufficient acceptance and resolution to identify exclusive reactions, a requirement imposed by the amplitude analysis needed to determine the J^{PC} quantum numbers of the produced mesons. The photons of particular interest are those resulting from $\pi^0 \to \gamma\gamma$ and $\eta \to \gamma\gamma$ decays. Photoproduction data at 9 GeV are sparse and mainly come from bubble chamber experiments, in which reconstruction of final states with multiple neutral particles is impossible. Such final states are expected to make up 60% of the photoproduction cross section, underscoring both the need and discovery potential for neutral particle reconstruction. GlueX will run in a dedicated experimental hall (Hall D) at Jefferson Lab, to be constructed as part of the 12 GeV upgrade to the lab.

2.1 The GlueX Detector and Barrel Calorimeter

The GlueX detector design is ideally suited for a fixed-target photoproduction experiment. The 2.2 T solenoidal magnetic field traps low-energy electromag-

* Corresponding author. Tel.: +1 306 585 4653; fax: +1 306 585 5659
   Email address: `leverinb@uregina.ca` (B.D. Leverington).

netic background (e^+e^- pairs) generated in the target inside a small diameter beam hole that runs through the detector. The photon beam is incident on a 30-cm LH$_2$ target. The target is surrounded by a start counter made of plastic scintillator that provides event timing information, a cylindrical tracking chamber (CDC) and a cylindrical electromagnetic calorimeter (BCAL). Downstream of the target are circular planar tracking chambers (FDC) and a circular planar electromagnetic calorimeter (FCAL). A schematic of the detector is shown in Fig. 1; the two electromagnetic calorimeters are used to detect and determine the four-momentum of the aforementioned decay photons.
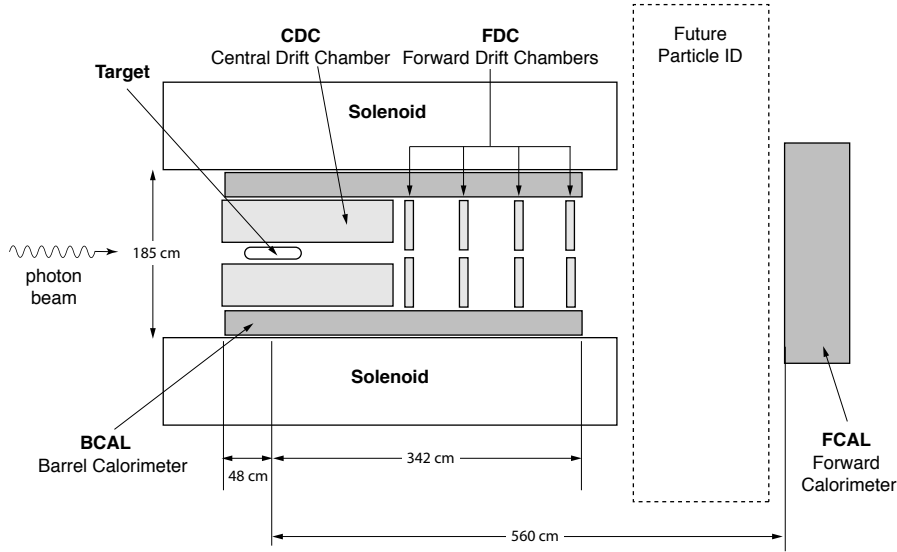

Fig. 1. Schematic of the GlueX Detector. The detector has cylindrical symmetry about the beam direction. The detector subsystems and the dashed lines at angles (with respect to the beam direction) 10.8° through 126.4° are referenced in the text. The start counter is not shown for clarity.

The BCAL is shown schematically in Fig. 2. The dimensions of this calorimeter are driven by the volume required for charged particle tracking and the bore dimensions of the solenoidal magnet. The BCAL design is based on that of the electromagnetic calorimeter used in the KLOE experiment at DAΦNE-Frascati, which also operated in a solenoidal magnetic field [1,2,3]. The BCAL and KLOE calorimeters both employ a lead/scintillating-fibre (Pb/SciFi) matrix of similar length with photosensors at either end to provide energy (ADC) and time (TDC) measurements. The diameter of the KLOE calorimeter is about three times that of the BCAL.

The relevant parameters that determine the π^0 and η mass resolutions are the photon energy (E) and the polar and azimuthal position resolutions (σ_θ and σ_ϕ). The energy resolution (σ_E) depends on the number of photoelectrons (N_{pe}) yielded by the photosensors, based on the collected light. The photo-
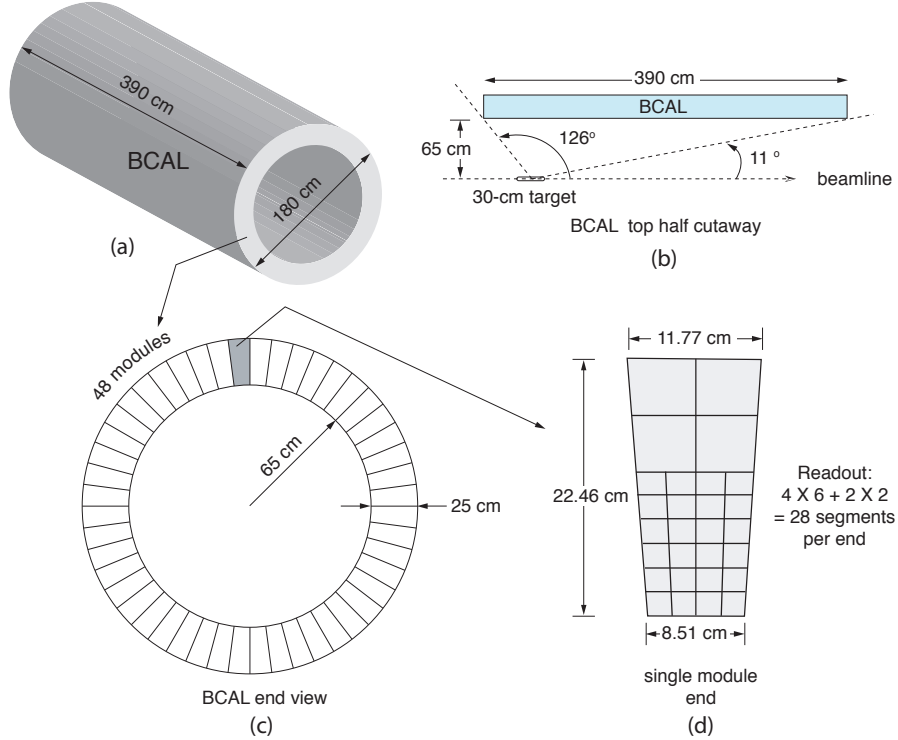
Fig. 2. The GlueX BCAL. (a) BCAL schematic; (b) a BCAL module side view; (c) end view of the BCAL showing all 48 modules and (d) an end view of a module showing readout segmentation. Details are given in the text.

electron statistics are strongly dependent on the stochastic fluctuations of the energy deposited by the electromagnetic shower in the scintillating fibres of the calorimeter modules. In addition, the number of photoelectrons collected depends on the fraction of photon shower energy deposited in the fibres, the efficiency with which the resulting scintillation light is captured in and transmitted down the fibre to the photosensor, and the photon detection efficiency of the photosensor. The photon position is determined by the readout segmentation in the azimuthal direction and the difference in arrival time (ΔT) of the scintillation light between the two ends of the barrel. The resolution in the time difference ($\sigma_{\Delta T}$), and therefore the polar angle resolution, also depend on the number of photoelectrons. The former is a critical input into the momentum resolution for photons and for the particle identification for charged particles, in conjunction with trajectories from the drift chambers. As such, the time difference analysis is reported in this paper as being more representative of the intrinsic BCAL resolution and independent of any external timing reference. Other parameters of relevance for extracting physics are adequate segmentation to avoid multiple occupancy, good linearity and a sufficiently low-energy threshold for photon detection.

The performance metrics for these quantities were set by simulating hadronic photoproduction at GlueX energies using PYTHIA [4] and also by simulat-

ing several of the signature reactions expected to yield exotic mesons. These studies included a GEANT-based simulation [5] of the entire GlueX detector response, including detector material and cabling, photon reconstruction and kinematic fitting. The PYTHIA simulations indicate that 70% of the produced photons with energies up to about 2 GeV will be incident on the BCAL. The photon population in the BCAL for one of the signature reactions, $\gamma p \rightarrow \eta \pi^0 p \rightarrow 4\gamma p$, where the distribution in $\eta \pi^0$ mass was uniform from 1.0 to 2.0 GeV/c^2 and uniform in decay angles, is shown in Fig. 3. The distribution of photons is plotted as a function of position from the upstream end of the BCAL; the photons predominantly populate the downstream end of the BCAL. The target occupies the region $z = 33 - 63$ cm. Also shown is the average energy as a function of z with higher energy photons being more forward. The integrated thickness of the BCAL matrix, in number of radiation lengths, traversed by photons incident at various positions along the length of the BCAL is also shown. Note that there is a narrow ($\sim 1°$) angular range near $11°$ where the photon trajectory intercepts a small number of radiation lengths of the Pb/SciFi matrix. Photons with angles less than $10°$, with respect to the beam direction, are detected in the FCAL.
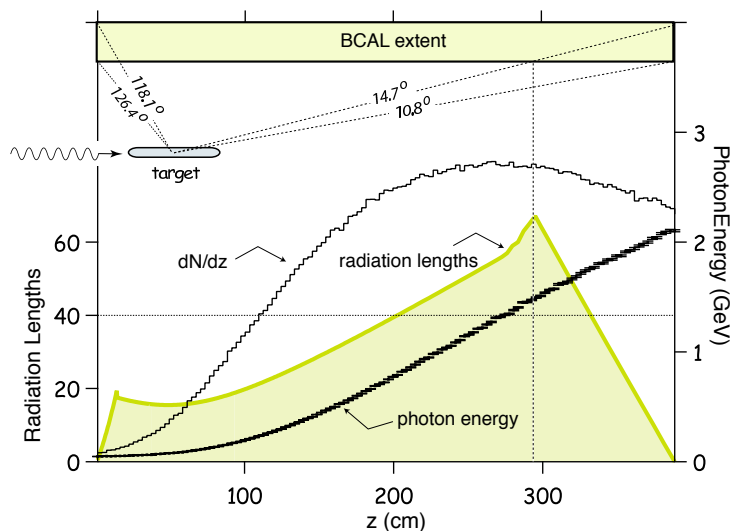

Fig. 3. The distribution of photons, their energy and integrated path length through the Pb/SciFi matrix as a function of position along the length of the BCAL for one of the GlueX signature reactions, $\gamma p \rightarrow \eta \pi^0 p \rightarrow 4\gamma p$, is shown. The target position and angular range subtended by the BCAL are also presented.

Moreover, the segmentation shown in Fig. 2d leads to double-occupancy in less than one-percent of events with two or more photons incident on the BCAL. This segmentation is also required for adequate determination of the azimuthal angle of tracks as well as for providing information on the energy deposition profile in depth, for good cluster identification. Additionally, studies of the lowest energy photons in high-multiplicity reactions that are expected to yield exotic hybrids such as $\gamma p \rightarrow b_1(1235)\pi n \rightarrow 2\pi^+\pi^-2\pi^0 n$ indicate that

an energy threshold of 40 MeV suffices.

Finally, it is important to point out differences in the GlueX and KLOE applications of barrel calorimetry. KLOE is a symmetric colliding beam experiment with the intersection region at the centre of its barrel calorimeter. As a result, that calorimeter is illuminated symmetrically and nearly uniformly by photons having energies, on average, between 100 and 200 MeV and with very few photons greater than 400 MeV. On the other hand, GlueX is a fixed target experiment, resulting in a highly asymmetric photon distribution: 30% of the photons in the BCAL will have energies considerably higher than 500 MeV. Despite these differences, the KLOE experience provides valuable guidance in the design and construction of the BCAL. The achieved KLOE energy resolution of $\sigma_E/E = 5.7\%/\sqrt{E(\text{GeV})}$ and time resolution of $54/\sqrt{E(\text{GeV})} \oplus 50$ ps are also adequate to achieve the GlueX physics requirements, as indicated by our simulation studies. The extracted resolutions are a direct result of the internal Pb/SciFi matrix geometry such that similar resolutions should be expected for the BCAL [6].

2.2 Module Geometry

Table 1 summarizes the salient features of the BCAL. These parameters are based on the KLOE experience, detailed GEANT-based simulations and tests of a full-scale prototype with charged particles, photon beam and cosmic rays. Aside from the attenuation length, the SciFi parameters are not brand specific but rather represent the generic parameters of double-clad fibres. The latter have a higher capture ratio compared to single clad fibres, such as used in KLOE. The nominal increase in capture ratio is over 50%, thus resulting in a similar increase in the number of photoelectrons, which can be important for low energy photons incident on the BCAL and the corresponding thresholds of the detector.

The first prototype module (Module 1), used in the beam test described in this paper, was constructed of alternating layers of 99.98% pure lead of 0.5 mm thickness that were grooved ("swaged"), creating channels to accommodate the fibres. This was accomplished by passing the lead sheets between the two grooved rollers of a custom-designed machine thereby creating the channels by plastic deformation of the lead. The fibres were obtained from PolHiTech[1] and are type PHT-0044 double-clad scintillating fibres of 1 mm diameter. These were bonded in the lead channels with Bicron-600[2] optical epoxy. The thickness of the module is 23 cm, its length is 400 cm and the width is 12 cm with the internal matrix geometry as indicated in Fig. 4. The matrix was built

---

[1] PolHiTech SRL, 67061 Carsoli (AQ), Italy (www.polhitech.it)
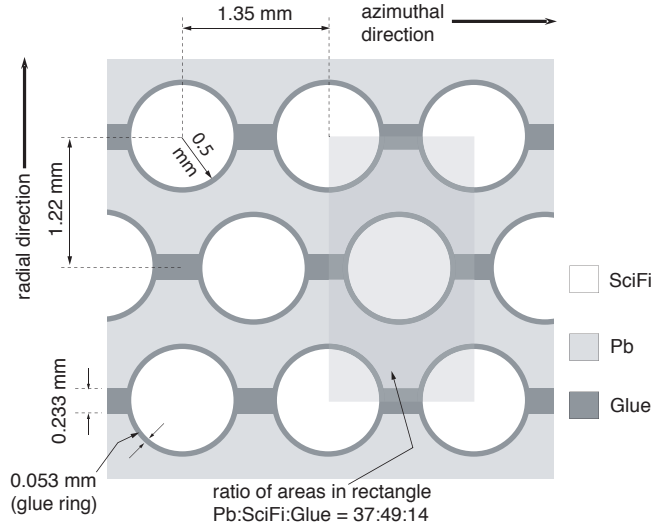[2] Saint-Gobain Crystals & Detectors, USA (www.bicron.com)

Fig. 4. The BCAL fibre matrix showing the placement of 1 mm diameter fibres in the azimuthal and radial directions. The dimensions of the azimuthal and radial pitch, the glue box between the lead sheets and the glue ring around the fibres were determined from the prototype module using a measuring microscope. Particle tracks would appear to enter the matrix from the bottom. More details are given in Ref. [11].

upon an aluminum base plate of 2.54 cm thickness that was further supported by a steel I-beam for added stiffness and ease of handling. Module 1 was not machined along its long sides at the 7.5° indicated in Fig. 2 and retained its rectangular profile from production. In contrast, the two ends of the module, where the read-out system was attached, were machined and polished. Visual inspection revealed that only eight of the approximately 17 000 fibres had been damaged in handling and construction. No optical defects affecting light transmission were observed in the other fibres.

3 Beam Test

The goals of the beam test were to measure the energy, timing and position resolutions of the BCAL module as well as the response of the module at different positions along its length and at various angles of the incident beam. The detailed analysis and results reported in this paper are for the module perpendicular to the beam ($\theta = 90°$) with the beam incident at its centre ($z = 0$ cm).

3.1 Experimental Facility

The beam test took place in the downstream alcove of Hall B at the Thomas Jefferson National Accelerator Facility (Jefferson Lab). In order to accommodate the module with its support frame, read-out system and cables, an additional platform was installed in front of the alcove. This expanded space allowed for the measurements with the photon beam perpendicular to the module, as well as providing a greater range of lateral and rotational degrees of freedom for the module when positioned inside the alcove. However, as illustrated in Fig. 5, the relative dimensions of the alcove and platform, with respect to the length of the module, still allowed for only a limited range of positions and incident angles that could be illuminated by the beam. Measurements, when the module was on the platform and oriented perpendicularly to the beam, were possible for relative positions of the beam spot between −100 cm to +25 cm with respect to the centre of the module. Within the alcove, the angular range was limited to angles 40° and less, and a length scan was carried out between −190 cm to −15 cm. The module was mounted on a cart that could be remotely rotated with good precision to the required angle. Lateral movements of the module with respect to the beam required a hall access for manual positioning.
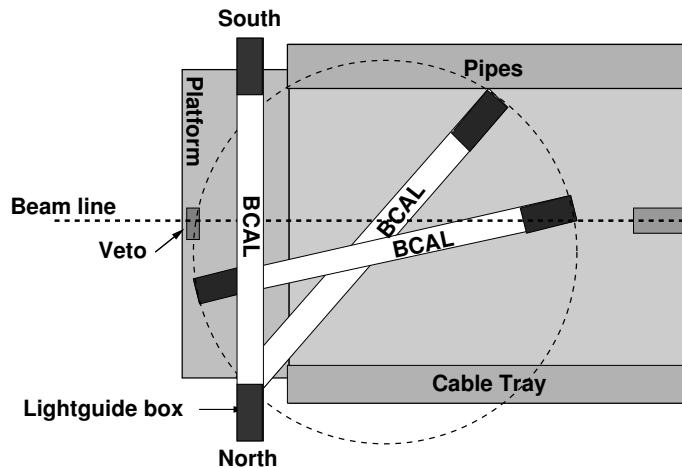

Fig. 5. Diagram of the Hall-B downstream alcove with schematic placements of the BCAL module. The drawing is not to scale.

The primary electron beam energy from the CEBAF accelerator at Jefferson Lab was $E_0 = 675$ MeV and the current was 1 nA for most of the measurements. The electron beam was incident on a thin target (the "radiator") located just upstream of the magnetic spectrometer (the "tagger"). The energies of the electrons scattered from the radiator were measured, thus providing timing and momentum information for the associated bremsstrahlung photons with a spectrum of energies from 150 MeV up to 650 MeV, as described below. The photon beam was collimated with a 2.6 mm collimator reducing the

flux after collimation to 6.5% of its orginal value, resulting in a beam spot of virtually uniform density with a diameter of 1.9 cm on the BCAL module. The distance from the radiator to the collimator and the collimator to the BCAL were 5.8 m and ∼39 m, respectively. See Ref. [15] for more details on the Hall B tagger.

The Hall B tagger system determines the electron momentum information from 384 individual scintillator paddles, called E-counters, with a phototube on one end. Each of these counters is arranged to cover constant momentum intervals of $0.003E_0$ and to physically overlap with its adjacent neighbour by 1/3 of its width, thus creating 767 individual photon energy bins and providing an energy resolution of $0.001E_0$. The timing information, on the other hand, is provided by 61 individual scintillator counters, called T-counters, with photo-tubes attached to both ends. The T-counters are classified in two groups. The first 19 (narrower) counters cover 75% to 90% of the incident electron energy range and the remaining 42 counters cover the 20% to 75% range.

3.2   Readout and Electronics

The module was divided into 18 readout segments, each with dimensions $3.81\times$ 3.81 cm^2. This segmentation comprised six rows in depth and three columns vertically with respect to the beam, as shown in Fig. 6. Acrylic light guides having a square profile and with a 45° mirrored surface channelled the light from the fibres to the PMTs that were placed perpendicularly to the fibre direction on both the North and South ends of the module, as shown in Fig. 7. The staggered, vertical placement of the PMTs was due to their diameter of 5 cm being larger than the 3.81 cm width of the readout segment size. Large, rectangular silicone sheets, 2.5 mm thick, were used to interface the light guides with the module and smaller, circular, 2.5 mm thick, silicone cookies coupled the PMTs to the light guides. The readout ends and all their components were enclosed in an aluminum box painted black with the top covered by Tedlar® [3] PVF to maintain light-tightness. The shower profile was such that most of the energy, nearly 90%, was deposited in the first 12 cm of the BCAL and the largest number of photoelectrons originated in that part of the module. For this reason, the three upstream columns of Fig. 6 were read out using Philips[4] XP2020 photomultiplier tubes. These tubes were selected for their good timing characteristics. The last three rows were read out using Burle[4] 8575 PMTs.

The bases for the PMTs were designed with dual BNC outputs on the anode.

---

[3] Tedlar® is a registered trademark of E. I. du Pont de Nemours and Company or its affiliates.
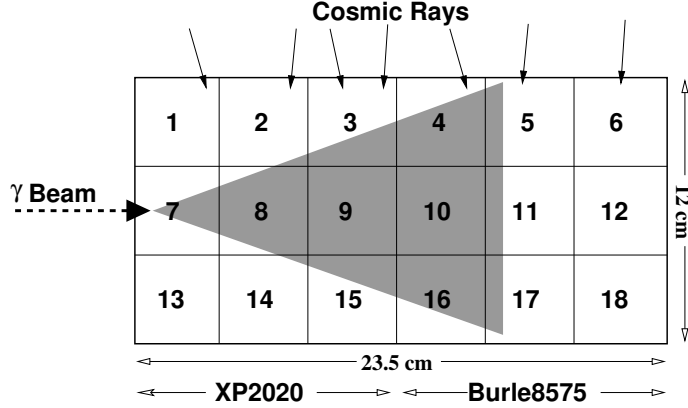[4] PHOTONIS SAS, Brive, France (www.photonis.com)

Fig. 6. The segmentation and readout for the BCAL module as viewed from its North end. The lead/scintillating fibre matrix would appear to be rotated by 90° with respect to Fig. 4. The electromagnetic shower that develops in the module approximately forms a cone shape and is illustrated with the shaded triangle in the figure. A very small percentage of the energy is deposited in the outer segments or leaks out the sides.

(a) light-guide box in the alcove   (b) drawing of the light-guide box
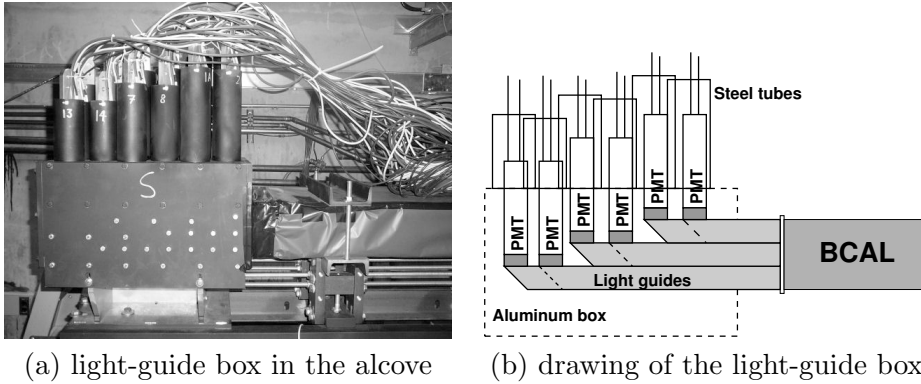
Fig. 7. (a) The box that encloses the 18 light guides and PMTs with cables attached for the South end of the BCAL module is shown. (b) The module is entirely wrapped in Tedlar® on the right and pressed against the light guides using a silicone sheet, as described in the text.

The signals were sent to a CAEN C207 equivalent leading edge discriminator and from there they were sent directly to a JLab F1 TDC [16] that was used to record the timing of the signals. The sum of the discriminator outputs was sent to a second discriminator, the threshold of which was set to require signals from at least four PMTs from each end of the module. The threshold logic pulse from either end (North OR South) of the module and the Master OR (MOR) signal from the T-counters of the tagger defined the trigger for the experiment. On average, the event rate was between 1 to 4 kHz for the duration of the beam test. A special electronics module was used to allow cosmic event triggers from scintillator paddles placed above and below the module as well as triggers from a pulser that were used to establish ADC pedestals, and were recorded concurrently with beam data. Signal amplitudes from the the second BNC output of the PMTs were digitized using CAEN V792 ADCs.

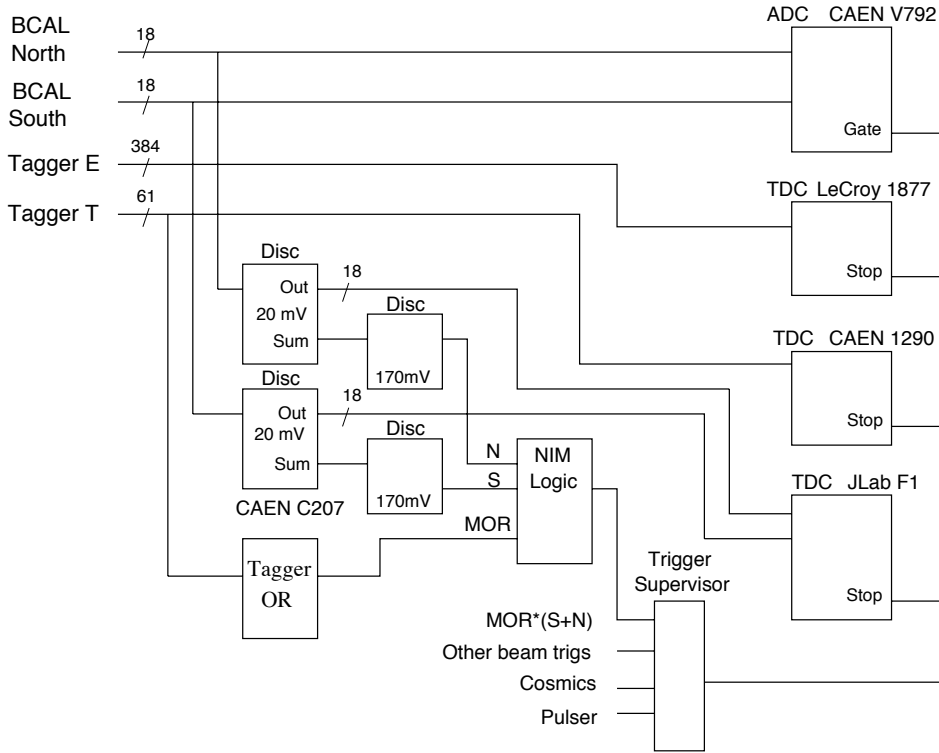The complete logic diagram is shown in Fig. 8.

Fig. 8. The logic diagram for the BCAL Hall-B beam test electronics. It should be noted that segments 1 and 13 did not contribute to the trigger, and this explains the apparent discrepancy between the 18 outputs of the discriminator and the sum output (which is just 16).

4   Energy Resolution

4.1   Gain balancing and energy calibration

With the module divided into 18 segments on each of the North and South sides, 36 PMTs were utilized in total. By adjusting the PMT supply voltage, an initial, relative balancing of the PMT gains was performed using cosmic data during the setup stage such that the means of the cosmic ADC spectra were nominally within ten percent of a certain value; only a couple channels deviated from this value by up to a factor of two. Further adjustments to the gains were done in software during the analysis: two different methods were used to determine the relative gain of each PMT and the subsequent absolute energy scale.

The first calibration algorithm adjusted the 36 gain constants by minimizing the fractional width of the distribution of the difference between the recon-

11

structed BCAL energy and the tagged photon beam energy. This ratio, D, is defined as

$$D = \frac{E_{\text{BCAL}} - E_{\text{BEAM}}}{E_{\text{BEAM}}}, \tag{1}$$

where E_{BCAL} is defined as

$$E_{\text{BCAL}} = K \cdot \sqrt{\left(\sum_{i=1}^{18} \frac{N_{\text{ADC},i}}{C_{\text{N},i}}\right)\left(\sum_{i=1}^{18} \frac{S_{\text{ADC},i}}{C_{\text{N},i}R_{\text{S/N},i}}\right)} \tag{2}$$

E_{BCAL} is the reconstructed energy in the BCAL module and E_{BEAM} is the photon energy measured in the tagger. The overall calibration constant, K, is the slope of the value under the square root versus the tagged photon energy. The North pedestal-subtracted ADC value, $N_{\text{ADC},i}$, is divided by the ADC balancing constant, $C_{\text{N},i}$. The South pedestal subtracted ADC value, $S_{\text{ADC},i}$, is divided by the product of the same balancing constant $C_{\text{N},i}$ and the means of the distributions of North ADC/South ADC's, $R_{\text{S/N},i}$ for the 18 segments. The scintillating fibres produce a narrow distribution for the ratio of ADC responses from the BCAL such that the 18 ratios, $R_{\text{S/N},i}$, can be used to reduce the overall number of free parameters for the gain balancing constants from 36 to 18. The reconstructed energy in the BCAL module is then the geometric mean of the balanced ADC values multiplied by K. D is recalculated in an iterative process as the balancing constants change, where each balancing constant is adjusted until D is minimized. The width of the distribution, σ_D, is the energy resolution, σ_E/E, for the module.

In order to provide a more transparent functional dependence, Eq. 2 can be re-written as

$$E_{\text{BCAL}} = \sum_{i=1}^{18} E_i \tag{3}$$

where

$$E_i = \sqrt{E_{\text{N},i} \cdot E_{\text{S},i}} \tag{4}$$

and $E_{N,i}$ and $E_{S,i}$ are the calibrated energies corresponding to the ith segment on the North and South side, respectively.

A plot of D vs. E_{BEAM} can be seen in Fig. 9. This shows how well the energy in the BCAL can be reconstructed and the PMT gains balanced. The deviations from zero below 200 MeV are most likely due to background that could not
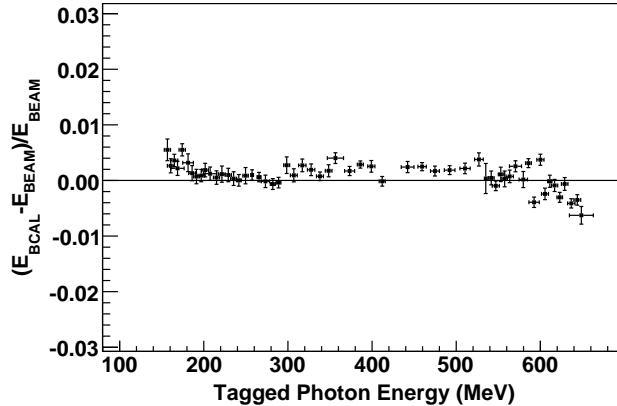
Fig. 9. $D = (E_{\mathrm{BCAL}} - E_{\mathrm{BEAM}})/E_{\mathrm{BEAM}}$ is shown after gain balancing and calibration. Notice that the deviations from zero are typically less than 0.5%.

be removed from the ADC spectra. The deviations from zero above 575 MeV are probably due to electromagnetic shower leakage from the module at these higher energies.

The second calibration algorithm used cosmic-ray data collected during and immediately after the beam test to balance the gain in each of the segments. This algorithm was used to cross check the method described above. A uniform population of minimum ionizing particles will deposit similar amounts of energy in each of the segments in a column and should produce similar ADC responses in the segments. The ratio of North to South ADC response was measured and each individual segment was balanced with respect to the others. An overall ADC calibration constant was applied afterwards. This method was found to work well, in principle, but the low statistics in each segment and the inability to remove "corner clipping" (cosmic muons grazing the corner segments) from the outer segments produced results with a worse resolution than the photon beam data. For this reason, the minimization algorithm method was employed for the final analysis pass of the energy and timing resolutions – with the cosmic balancing used only as a cross check – yielding quite satisfactory and consistent results.

4.2 Energy resolution results

The calibrated spectra for D were derived from the energy difference minimization algorithm calibration for each tagger timing counter and were fitted by a Gaussian function. A typical spectrum and its fit are shown in Fig. 10, this one for timing counter 40, corresponding to a beam energy of 273 MeV.

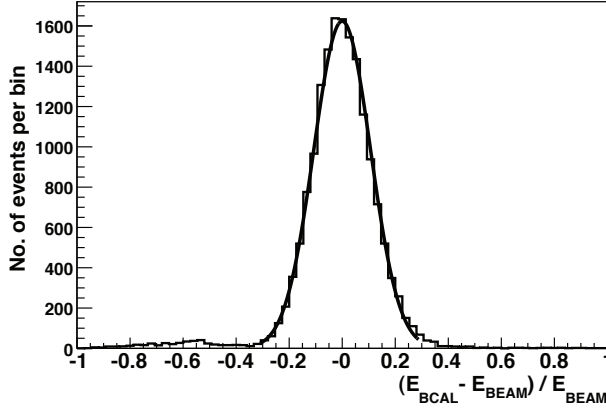Subsequently, the energy resolution was extracted for all timing counters and

13

Fig. 10. The calibrated spectrum for D is shown for timing counter 40, corresponding to a beam energy of 273 MeV. The solid line is a Gaussian fit to the data.

is shown in Fig. 11, plotted as a function of the tagged photon beam energy, for the data at $\theta = 90°$ and z=0 cm. The fit to the data is also shown in Fig. 11, resulting in

$$\frac{\sigma_E}{E} = \frac{5.5\%}{\sqrt{E(\text{GeV})}} \oplus 2.4\%, \tag{5}$$

where the $\oplus$ indicates addition in quadrature. Small variations in the fits produced relatively large variations in the floor term ($2.4 \pm 1\%$) but little variation in the stochastic term ($5.5 \pm 0.1\%$).
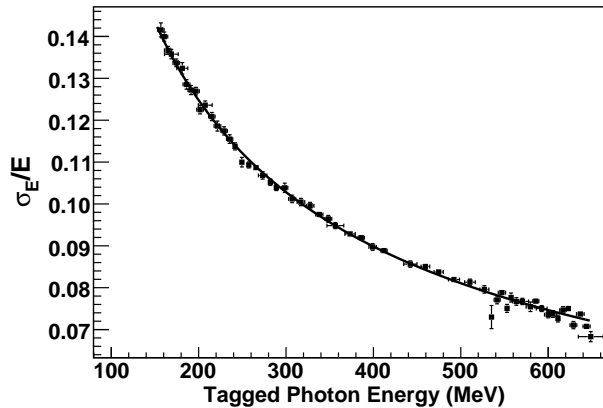

Fig. 11. Energy resolution vs. E_{BEAM} for photons for $\theta = 90°$ and $z = 0$ cm. The fit gives $\sigma_E/E = 5.5\%/\sqrt{E(\text{GeV})} \oplus 2.4\%$. The fit of Fig. 10 corresponds to the 40th datum from the right (19th from the left) in this figure.

In general, the energy resolution of an electromagnetic calorimeter is expressed

in the form:

$$\frac{\sigma_E}{E} = \frac{a}{\sqrt{E(\text{GeV})}} \oplus b \oplus \frac{c}{E(\text{GeV})}. \tag{6}$$

The $a/\sqrt{E}$ term contains the combined effect of sampling fluctuations and photoelectron statistics. It is commonly referred to as the stochastic term. The $1/\sqrt{E}$ dependence is expected from the fact that the fluctuations are proportional to the number of particle tracks, n, that cross the active material; n has a Poisson distribution with a variance $\sqrt{n}$. Since the energy of a shower is proportional to n, the contributions to the resolution σ_E/E due to the stochastic fluctuations is proportional to $1/\sqrt{E}$. The KLOE collaboration concluded that the photon statistics from the light yield of their calorimeter ranges from $1.6\%/\sqrt{\text{E(GeV)}}$ [17] up to $2.7\%/\sqrt{\text{E(GeV)}}$[18] and, therefore, contributes very little to the resolution since it is added in quadrature to the sampling contribution. Indeed, the stochastic fluctuations in sampling dominate the resolution.

The constant term, b, in Eq. 6, originates from all other energy-independent sources that contribute to uncertainties in the energy reconstruction. These sources can be mechanical imperfections, material defects, segment-to-segment calibration variations, non-uniformity of response, instability with time and shower leakage. Much work has gone into removing any of these effects during the construction of the BCAL module, throughout the beam test, and in any subsequent analysis. It has been seen in simulations that the leakage is nearly constant with energy over most of the energy range of the beam tests, except at the low end where it was slightly reduced and at the high end where it increased moderately.

If contributions from the noise term, c/E, existed, they would be from electronics noise and pileup in high-rate environments. This term increases at lower energies but has not been observed to contribute in the beam test analysis as both the rates and noise were low. Fits to the beam test data including this term produce almost identical stochastic and constant terms with values for c consistent with zero.

The stochastic coefficient $a = 5.5\%$ in Eq. 5 compares very well with the corresponding one from KLOE, reported as $a = 5.7\%$. The KLOE calorimeter and BCAL Module 1 as read out in the beam test have similar sampling fractions and photostatistics. Although the production readout for BCAL will be different, the beam test setup resulted in benchmark metrics for any future upgrades to the BCAL matrix structure, such as increasing the sampling fraction in the inner layers to improve low energy photon detection for critical regions of exotic hybrid production phase space and producing a better energy resolution.

As mentioned above, the stochastic fluctuations in sampling dominate the resolution. This being the case, there should be little effect of the shower position along the module (z) on the energy resolution, because attenuation only affects the number of photoelectrons at the read-out ends of the module and is compensated for by the double ended read-out of the module. On the other hand, increasing the photon beam energy results in more particle tracks over a greater depth of the shower profile generated within the module, therefore more fibre layers are intercepted by more particle tracks. The expectation, then, is that the resolution will improve with increasing photon energy but remain nearly independent of the position of the beam spot. This can be seen in Fig. 12, where the energy resolution for photon energies from 225 MeV to 575 MeV for three z-positions at normal incidence is shown.
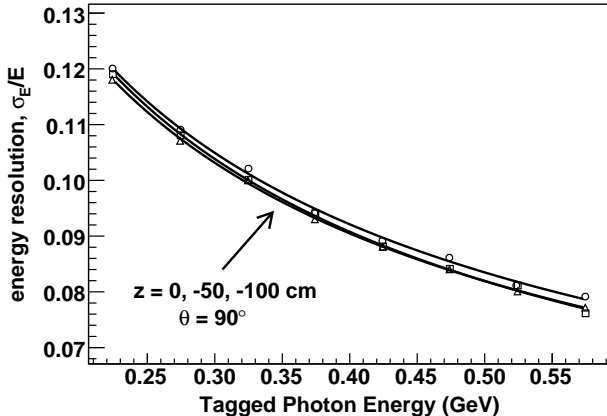

Fig. 12. The energy resolution for three z-positions. The fits are to $a/\sqrt{E} \oplus b$ and are virtually indistinguishable from each other.

Finally, b a reasonable indicator of the intrinsic constant term in the energy resolution of the BCAL. However, the maximum energy of the photon beam test was too low to determine it precisely, as the constant term contributes negligibly to the resolution at a few hundred MeV when added in quadrature to the stochastic. Nevertheless, since approximately 30% of the photons in GlueX will have energies above 500 MeV, efforts to minimize the constant term and extract it more accurately will be fruitful.

4.3 Sampling fraction and energy

The sampling fraction – the fraction of energy deposited in the SciFi's – can be expressed as a ratio with respect to either the total energy deposited in the BCAL module (f) or the incident photon energy (f_γ). These quantities, however, are difficult to measure in an experiment but fairly simple to simulate. A GEANT 3.21 simulation was developed to that end, based on modelling

16
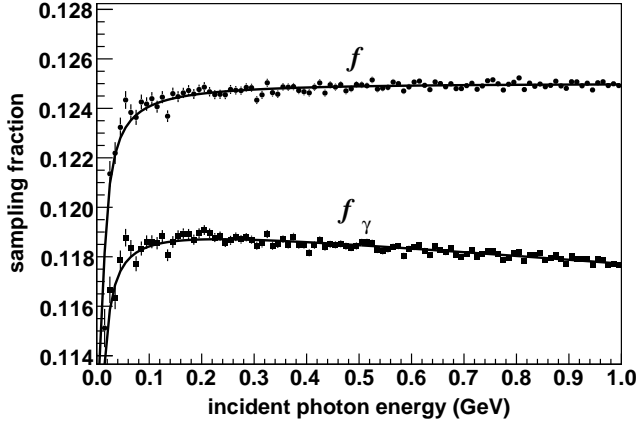
(a)
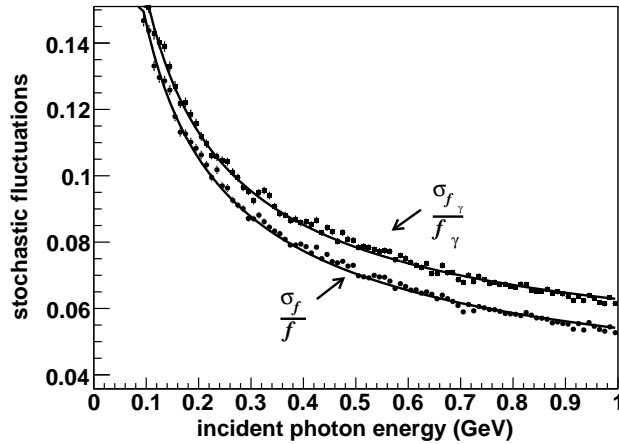
(b)

Fig. 13. (a) The photon energy sampling fraction, f_γ, and deposited energy sampling fraction, f, are shown from simulation for $\theta = 90°$. The data are fit to $a_0/E + a_1 E + a_2$ functions, which were chosen among the simplest functions that described the data well. (b) The sampling fluctuations of the module, $\sigma_{f_\gamma}/f_\gamma$ and σ_f/f are plotted from simulation. The data are fit to $a/\sqrt{E} \oplus b$ functions with $a_{f_\gamma} = 4.56\%$, $b_{f_\gamma} = 1.55\%$, $a_f = 4.45\%$ and $b_f = 0.93\%$.

the BCAL as a standalone package and independent from the previously mentioned simulations. Individual fibre and epoxy volumes were programmed into the Monte Carlo with the appropriate Pb:SciFi:Glue ratios and material properties resulting in the geometry shown in Fig. 4.

Simulations indicate that f_γ decreases as a function of photon energy due to leakage and this is shown in Fig. 13a, with the loss being linear above 200 MeV. It should be noted that the size of the module will primarily affect only f_γ in the sense that a smaller module will result in a smaller f_γ due to energy from the electromagnetic shower leaking outside the module. On the other hand, f

17

depends only on the energy deposited in the matrix itself and is independent of the incident photon energy or overall geometry of the module. The deviation from linearity at low energy is probably due to the fact that more of the low energy electrons and positrons from the electromagnetic shower stop in the lead before being sampled by the scintillating fibres. One would expect this reduction in both sampling fractions and this is what was observed.

The sampling fluctuations, σ_f/f, can be seen in Fig. 13b. These are the dominant contributor to the energy resolution, at about $4.5\%/\sqrt{E(\text{GeV})}$. Subtracting the simulated sampling fluctuation contributions from the measured energy resolution yields photoelectron statistics contribution to the energy resolution of about $3.1\%/\sqrt{E(\text{GeV})}$. This is similar to the estimated value of $\sim 2.7\%/\sqrt{E(\text{GeV})}$ from a KLOE beam test [18].

5 Timing and Position Resolution

The time difference of the BCAL will provide position information for neutral particles, which is needed to reconstruct their four-momentum. The position resolution is related to the time difference resolution by the effective speed of light within the calorimeter. Thus, by using measurements of the effective speed of light ($c_{\text{eff}} = (16.2 \pm 0.4)$ cm/ns in Table 1) from a previous beam test at TRIUMF [10], the position resolution of the calorimeter can be easily extracted.

The time difference resolution will be of the form:

$$\sigma_{\Delta T/2} = \frac{c}{\sqrt{E(\text{GeV})}} \oplus d. \tag{7}$$

In general, the constant term, d, in Eq. 7 is a result of residual calorimeter miscalibrations, but some fraction is also due to the finite width in z of the beam, which will contribute to the time difference resolution. With the beam width being $l \sim 1.9$ cm, the flat and square distribution of the beam contributes $(l/c_{\text{eff}})/\sqrt{12} = 30$ ps to the resolution.

The double-ended readout of the BCAL allowed for time difference measurements to be made, but because leading edge discriminators were used the timing had a dependence on pulse height which required a time-walk correction. A plot of ADC versus TDC for segment 8 can be seen in Fig. 14. Fits with a function of the form $p_0/\sqrt{\text{ADC}} + p_1$ were performed, as the time delay due to signal amplitude in leading edge discriminators follows this form. The fit parameter p_1 is a constant term indicating the timing offset of the partic-

18

ular readout segment from the tagger MOR timing signal. Parameter p_0 also varies depending on the particular readout segment but has a nominal value of ~ 35 ns $\cdot$ GeV$^{1/2}$. The fit is poor for the downstream segments, specifically segments 6 and 18 where the statistics are low, as there is very little energy deposited there and the fluctuations are consequently large. For this reason, most of the outer segments were not included in the timing analysis. Analysis of the timing data focused mainly on segments 7, 8, 9 and 10 where nearly 90% of the energy was deposited. ADC values lower than channel 350 were rejected, in the case of South 8, due to the resulting asymmetry from the walk correction at low ADC values, which caused distortions in the time difference resolution. This corresponds to 1 MeV of energy deposited in the segment or 0.125 MeV deposited in the fibres. Similar ADC cuts were made for the other segments depending on the distortion at the lower end of the ADC spectra. This results in a loss of efficiency at the lower energies but in a much improved time difference resolution over the whole tagger spectrum.
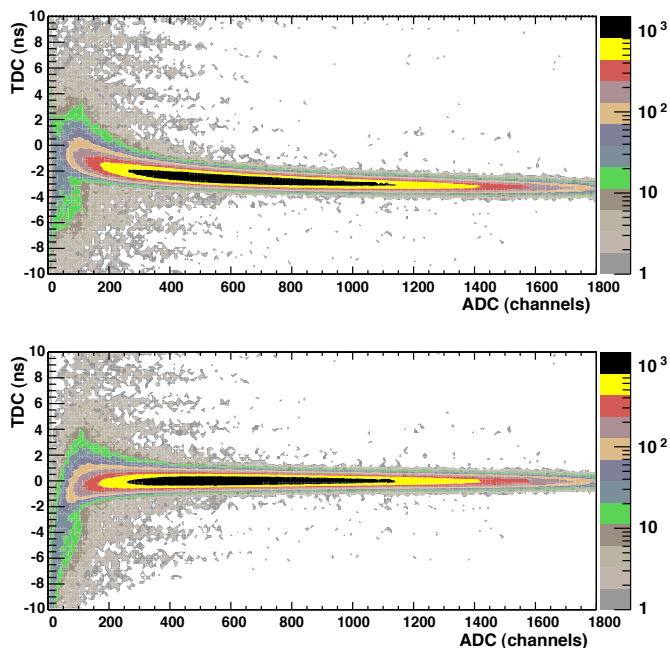

Fig. 14. ADC vs. TDC for segment South 8. The uncorrected time affected by the time walk due to the dependence on amplitude is seen in the top plot. The bottom plot shows the corrected time. The BCAL time was referenced with the tagger time. (colour online)

The timing for an event was found by summing the TDC values of all the segments in an event cluster, weighted by their energy; cuts on the ADC and timing determined whether a segment was included in the cluster. A cluster is defined by the energy weighted sum of the times of each segment such that

19

the time difference, ΔT, is expressed as:

$$\frac{\Delta T}{2} = \frac{1}{2} \frac{\sum_i E_i (T_{N,i} - T_{S,i})}{\sum_i E_i} \tag{8}$$

Subsequently, the walk-corrected spectra for each tagger timing counter were fitted by a Gaussian function. A typical spectrum and fit are shown in Fig. 15, this one for timing counter 40. All timing counter spectra were fitted in the same fashion, and the fit results are plotted on Fig. 16. From the subsequent fit in that figure, the time difference resolution including only the middle row segments 7, 8, 9 and 10 is found to be:

$$\sigma_{\Delta T/2,7-10} = \frac{75 \text{ ps}}{\sqrt{E(\text{GeV})}} \oplus 30 \text{ ps}. \tag{9}$$
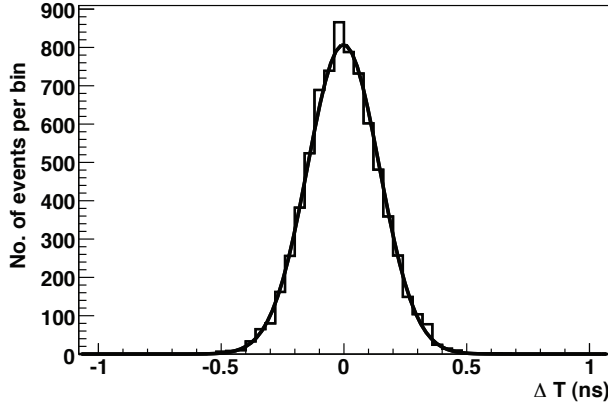

Fig. 15. The walk-corrected spectrum and Gaussian fit for timing counter 40. The solid line is a Gaussian fit to the data.

The floor term is equal to the finite width of the beam, as expected. This implies that the intrinsic time resolution of the BCAL is consistent with zero for the constant term. As the time difference resolution is dependent on the number of photoelectrons, the time difference resolution, $\sigma_{\Delta T/2,7-10}$, can be corrected to include the missing photoelectrons, after subtracting the beam width from the constant term, and is found to be

$$\sigma_{\Delta T/2} = \frac{70 \text{ ps}}{\sqrt{E(\text{GeV})}}. \tag{10}$$

This resolution also defines the position (z) resolution along the length of the module, since $\sigma_z = \sigma_{\Delta T/2} \cdot c_{\text{eff}}$. Therefore, based on the previous numbers, for a 1 GeV photon the determined position resolution is $\sigma_z = 1.1$ cm.
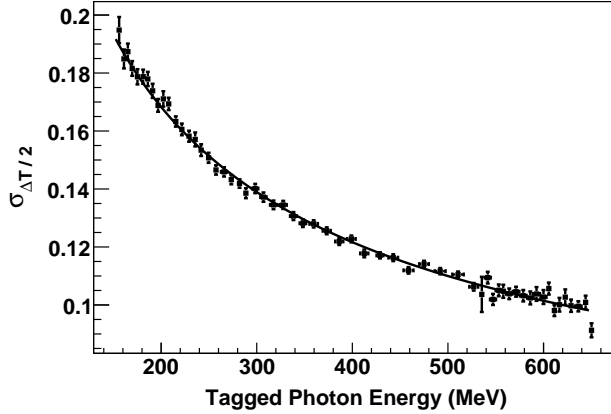
Fig. 16. The time difference resolution, in nanoseconds, for segments 7, 8, 9 and 10 as a function of energy. The fit gives $\sigma_{\Delta T/2} = 75 \text{ ps}/\sqrt{E(\text{GeV})} \oplus 30 \text{ ps}$. The fit of Fig. 15 corresponds to the 40th datum from the right (19th from the left) in this figure.

6 Determination of the number of photoelectrons

The number of photoelectrons per end of the prototype BCAL module, N_{pe}, was estimated at $z = 0$ cm and $\theta = 90°$. The distribution in the ratio, R, of the North to the South readout sums, for each of eight bins in beam energy, E_j, from 200 MeV to 600 MeV, was expressed as

$$R(E_j) = \frac{\sum_{i=1}^{18} E_{\text{N},i;j}}{\sum_{i=1}^{18} E_{\text{S},i;j}}. \tag{11}$$

This distribution was fitted to a Gaussian, yielding the mean and standard deviations, μ_R and σ_R. Using this ratio, instead of the individual summed energies, cancels out the effect of shower fluctuations that dominate the statistical variance of the individual sums for each readout end. Under the assumption that the number of photoelectrons per end is equal and is given by

$$N_{pe} = 2\frac{\mu_R^2}{\sigma_R^2}, \tag{12}$$

the photoelectron yield per end is plotted in Fig. 17 as a function of beam energy. Two linear fits are also shown, of the form:

$$N_{pe} = \alpha + \beta \cdot E(\text{MeV}). \tag{13}$$

The two-parameter fit yielded $\alpha = 14 \pm 4$ and $\beta = 0.634 \pm 0.01$ (MeV^{-1}) and is shown as the dashed line in Fig. 17. Notice that α is not zero as would
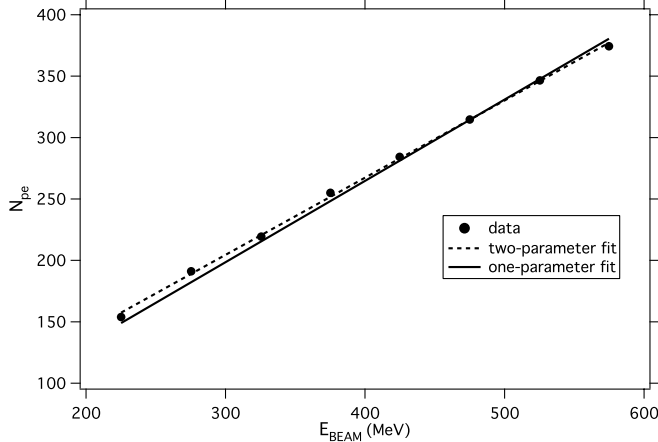
21

Fig. 17. The number of photoelectrons per end of the BCAL module is shown as a function of energy. Two linear fits are plotted: in the two-parameter fit both the slope and y-intercept are allowed to be free parameters in the fit, whereas for the one-parameter fit the y-intercept is held at zero as expected for $E = 0$ MeV. For more details see the text.

be expected at $E = 0$ MeV. This inconsistency may be due to some residual miscalibrations and/or due to the limited energy range of data available; whereas it is small relative to the number of photoelectrons extracted from the beam test at high energies, it is significant at the expected BCAL threshold ($N_{pe} = 25$ at $E = 40$ MeV). Therefore, a one-parameter fit, where α was held constant at zero, resulted in $\beta = 0.662 \pm 0.015$ (MeV^{-1}) and is shown as the solid line in Fig. 17. Since the second fit corresponds to the physical situation expected at $E = 0$ MeV, that β was used in all calculations below. Indeed, using that value and Eq. 13 and extrapolating to 1 GeV results $N_{pe} = 662 \pm 15$ photoelectrons per end. This analysis was based on the middle row of six readout segments (numbers 7-12) where the majority of light is produced. For the highest energy point (575 MeV) in Fig. 17, the number of photoelectrons is 381 ± 8.

Another approach is to apply the ratio technique to each of the 18 segments of the BCAL module to obtain a number of photoelectrons per segment and then sum:

$$R'(E_j) = \sum_{i=1}^{18} \frac{E_{N,i;j}}{E_{S,i;j}}. \tag{14}$$

The total number of photoelectrons in segments 7 through 12 of the middle row of the module was determined and extended to include all readout segments, resulting in $N_{pe} = 440 \pm 8$ at 575 MeV. Using this, the above value of $N_{pe} = 662 \pm 15$ at $E = 1$ GeV, obtained from the summed energy method, was corrected with the scaling factor of $440/381 = 1.16$ (determined at $E = 575$ MeV) to account for the upper and lower readout rows and yielded

22

the final value of $N_{pe} = 768 \pm 17$ at 1 GeV. In comparison, KLOE reported $N_{pe} \sim 700$ per end at 1 GeV. While the BCAL module used double-clad scintillating fibres, potentially giving rise to approximately 50% more photo-electrons than KLOE, the latter had light guides combined with Winston Cone collectors that resulted in a higher transport efficiency than the light guides used in the beam tests described in this work. These could easily compensate for the increased capture ratio of the fibres in the BCAL case.

7   Summary and Conclusions

The first full-scale prototype module for the BCAL tested the construction techniques and the performance of the matrix under beam conditions. An energy resolution of $\sigma_E/E = 5.5\%/\sqrt{E(\text{GeV})}$ and a time difference resolution of $\sigma_{\Delta T/2} = 70$ ps$/\sqrt{E(\text{GeV})}$ ps were found from the Jefferson Lab beam test data. The number of photoelectrons at 1 GeV is approximately 770. The energy and timing resolutions meet the original design goals and the performance of the module closely matched that of a proven sampling calorimeter like that of KLOE. The analysis for the more demanding regions of module and beam geometries, near the end of the module and at small incident angles can now proceed having established the performance under more benign conditions and having the Monte Carlo simulations tested and anchored to the data.

8   Acknowledgements

Property	Value	Ref.
Number of modules[a]	48	
Module length[a]	390 cm	
Module inner cord[a]	8.51 cm	
Module outer cord[a]	11.77 cm	
Module thickness[a]	22.5 cm	
Module azimuthal bite[a]	$7.5°$	
Radial fibre pitch[b]	1.22 mm	
Azimuthal fibre pitch[b]	1.35 mm	
Lead sheet thickness[c]	0.5 mm	
Fibre diameter[c]	1.0 mm	[7]
First cladding thickness[c]	0.03 mm	[7]
Second cladding thickness[c]	0.01 mm	[7]
Core fibre refractive index[c]	1.60	[7]
First cladding refractive index[c]	1.49	[7]
Second cladding refractive index[c]	1.42	[7]
Trapping efficiency[c,d,e]	5.3% (min) 10.6% (max)	[7,8,9]
Attenuation length[b]	(307±12) cm	[10]
Effective speed of light[b], c_{eff}	(16.2±0.4) cm/ns	[10]
Volume ratios[b]	37:49:14 (Pb:SF:Glue)	[11]
Effective mass number[e]	179.9	[11]
Effective atomic number[e]	71.4	[11]
Effective density[e]	4.88 g/cm^3	[11]
Sampling fraction[f]	0.125	[12]
Radiation length[e]	7.06 g/cm^2 or 1.45 cm	[11]
Number of radiation lengths[e]	$15.5 X_0$ (total thickness)	[11]
Critical energy[e]	11.02 MeV (8.36 MeV)	[13,14]
Location of shower maximum[e]	$5.0 X_0$ ($5.3 X_0$) at 1 GeV	[13,14]
Thickness for 95% containment[e]	$20.3 X_0$ ($20.6 X_0$) at 1 GeV	[13,14]
Molière radius[e]	17.7 g/cm^2 or 3.63 cm	[14]
Energy resolution[b], σ_E/E	$5.5\%/\sqrt{E} + 2.4\%$	
Time difference res.[b], $\sigma_{\Delta T/2}$	$70 \text{ ps}/\sqrt{E}$	
z-position resolution[b], σ_z	$1.1 \text{ cm}/\sqrt{E}$ (weighted)	
Azimuthal angle resolution[f]	~ 8.5 mrad	
Polar angle resolution[f]	~ 8 mrad	

Table 1

BCAL properties. Superscript: a - design parameters of the BCAL specified for the final detector; b - quantities that have been measured; c - specifications from the manufacturer; d - from literature; e - parameter calculated from known quantities; f = parameter estimated from simulations. The number of radiation lengths as well as the resolutions in the table are all at $\theta = 90°$ incidence.

Figure Captions

Fig. 1. Schematic of the GlueX Detector. The detector has cylindrical symmetry about the beam direction. The detector subsystems and the dashed lines at angles (with respect to the beam direction) 10.8° through 126.4° are referenced in the text. The start counter is not shown for clarity.

Fig. 2. The GlueX BCAL. (a) BCAL schematic; (b) a BCAL module side view; (c) end view of the BCAL showing all 48 modules and (d) an end view of a module showing readout segmentation. Details are given in the text.

Fig. 3. The distribution of photons, their energy and integrated path length through the Pb/SciFi matrix as a function of position along the length of the BCAL for one of the GlueX signature reactions, $\gamma p \rightarrow \eta \pi^0 p \rightarrow 4\gamma p$, is shown. The target position and angular range subtended by the BCAL are also presented.

Fig. 4. The BCAL fibre matrix showing the placement of 1 mm diameter fibres in the azimuthal and radial directions. The dimensions of the azimuthal and radial pitch, the glue box between the lead sheets and the glue ring around the fibres were determined from the prototype module using a measuring microscope. Particle tracks would appear to enter the matrix from the bottom. More details are given in Ref. [11].

Fig. 5. Diagram of the Hall-B downstream alcove with schematic placements of the BCAL module. The drawing is not to scale.

Fig. 6. The segmentation and readout for the BCAL module as viewed from its North end. The lead/scintillating fibre matrix would appear to be rotated by 90° with respect to Fig. 4. The electromagnetic shower that develops in the module approximately forms a cone shape and is illustrated with the shaded triangle in the figure. A very small percentage of the energy is deposited in the outer segments or leaks out the sides.

Fig. 7. (a) The box that encloses the 18 light guides and PMTs with cables attached for the South end of the BCAL module is shown. (b) The module is entirely wrapped in Tedlar® on the right and pressed against the light guides using a silicone sheet, as described in the text.

Fig. 8. The logic diagram for the BCAL Hall-B beam test electronics. It should be noted that segments 1 and 13 did not contribute to the trigger, and this explains the apparent discrepancy between the 18 outputs of the discriminator and the sum output (which is just 16).

Fig. 9. $D = (E_{\text{BCAL}} - E_{\text{BEAM}})/E_{\text{BEAM}}$ is shown after gain balancing and calibration. Notice that the deviations from zero are typically less than 0.5%.

Fig. 10. The calibrated spectrum for D is shown for timing counter 40, corresponding to a beam energy of 273 MeV. The solid line is a Gaussian fit to the data.

Fig. 11. Energy resolution vs. E_{BEAM} for photons for $\theta = 90°$ and $z = 0$ cm. The fit gives $\sigma_E/E = 5.5\%/\sqrt{E(\text{GeV})} \oplus 2.4\%$. The fit of Fig. 10 corresponds to the 40th datum from the right (19th from the left) in this figure.

Fig. 12. The energy resolution for three z-positions. The fits are to $a/\sqrt{E} \oplus b$ and are virtually indistinguishable from each other.

Fig. 13. (a) The photon energy sampling fraction, f_γ, and deposited energy sampling fraction, f, are shown from simulation for $\theta = 90°$. The data are fit to $a_0/E + a_1 E + a_2$ functions, which were chosen among the simplest functions that described the data well. (b) The sampling fluctuations of the module, $\sigma_{f_\gamma}/f_\gamma$ and σ_f/f are plotted from simulation. The data are fit to $a/\sqrt{E} \oplus b$ functions with $a_{f_\gamma} = 4.56\%$, $b_{f_\gamma} = 1.55\%$, $a_f = 4.45\%$ and $b_f = 0.93\%$.

Fig. 14. ADC vs. TDC for segment South 8. The uncorrected time affected by the time walk due to the dependence on amplitude is seen in the top plot. The bottom plot shows the corrected time. The BCAL time was referenced with the tagger time. (colour online)

Fig. 15. The walk-corrected spectrum and Gaussian fit for timing counter 40. The solid line is a Gaussian fit to the data.

Fig. 16. The time difference resolution, in nanoseconds, for segments 7, 8, 9 and 10 as a function of energy. The fit gives $\sigma_{\Delta T/2} = 75$ ps$/\sqrt{E(\text{GeV})} \oplus 30$ ps. The fit of Fig. 15 corresponds to the 40th datum from the right (19th from the left) in this figure.

Fig. 17. The number of photoelectrons per end of the BCAL module is shown as a function of energy. Two linear fits are plotted: in the two-parameter fit both the slope and y-intercept are allowed to be free parameters in the fit, whereas for the one-parameter fit the y-intercept is held at zero as expected for $E = 0$ MeV. For more details see the text.

References

[1] M. Adinolfi et al., Nucl. Instr. Meth. A 461 (2001) 344.

[2] M. Adinolfi et al., Nucl. Instr. Meth. A 494 (2002) 326.

[3] M. Adinolfi et al., Nucl. Instr. Meth. A 482 (2002) 364.

[4] T. Sjöstrand, S. Mrenna and P. Skands, Pythia 6.4 Physics and Manual, Technical Report, Lund University, 2006.

[5] GEANT 3.21 Detector Description and Simulation Tool, CERN Program Library Long Writeup W5013, Geneva, 1993.

[6] R. Wigmans, Nucl. Instr. Meth. A 494 (2002) 277.

[7] St. Gobain Crystals, Paris, France, Scintillating Optical Fibers Brochure 605.

[8] C.P. Achenbach, arXiv:nucl-ex/0404008v1, 2004.

[9] Z. Papandreou, GlueX-doc-918-v2 (http://portal.gluex.org/, Documents, Public), Technical Report, GlueX Collaboration, 2007.

[10] G. Koleva, M.Sc. Thesis (U. of Regina), 2006; GlueX-doc-824-v2, Technical Report, GlueX Collaboration, 2006.

[11] Z. Papandreou, GlueX-doc-840-v2, Technical Report, GlueX Collaboration, 2007.

[12] B.D. Leverington, GlueX-doc-827-v3, Technical Report, GlueX Collaboration, 2007.

[13] M.J. Berger and S.M. Seltzer, Tables of energy losses and ranges of electrons and positrons, Technical Report, NASA, Washington, DC, 1964.

[14] B. Rossi, High Energy Particles, Prentice-Hall, Inc., Englewood Cliffs, NJ, 1952.

[15] D.I. Sober et al., Nucl. Instr. Meth. A 440 (2000) 263.

[16] F.J. Barbosa, E. Jastrzembski, J. Profitt, and J. Wilson, Nuclear Science Symposium Conference Record, 2002 IEEE, 1:135-139 vol. 1, 10-16, 2002.

[17] A. Antonelli et al., Nucl. Instr. Meth. A 35 (1995) 362.

[18] A. Antonelli et al., Nucl. Instr. Meth. A 379 (1996) 511.